JOURNAL OF GEOPHYSICAL RESEARCH, VOL. 111, A07307, doi:10.1029/2005JA011415, 2006



# Zonal winds in the equatorial upper thermosphere: Decomposing the solar flux, geomagnetic activity, and seasonal dependencies

Huixin Liu,[1] Hermann Lühr,[2] Shigeto Watanabe,[1] Wolfgang Köhler,[2] Vance Henize,[2] and Pieter Visser[3]

Received 9 September 2005; revised 15 March 2006; accepted 29 March 2006; published 15 July 2006.

[1] Using 3 years (2002–2004), over 16,400 orbits of measurements from the accelerometer on board the CHAMP satellite, we have studied the climatology of the equatorial zonal wind in the upper thermosphere. Several main features are noticed. The most prominent one is that the solar flux significantly influences both the daytime and nighttime winds. It overrides the geomagnetic activity effect, which is found to be rather limited to the nightside. An elevation of the solar flux level from $F10.7 \approx 100 \times 10^{-22}$ W m$^{-2}$ Hz$^{-1}$ to $F10.7 \approx 190 \times 10^{-22}$ W m$^{-2}$ Hz$^{-1}$ produces an eastward disturbance wind up to $\sim$110 m s$^{-1}$. This consequently enhances the nighttime eastward wind but suppresses the daytime westward wind. A seasonal variation with weaker wind (by over 50 m s$^{-1}$ at night) around June solstice than in other seasons has been observed regardless of solar flux and geomagnetic activity levels. The zonal wind is eastward throughout the night except around June solstice, where it ebbs to almost zero or turns even westward in the postmidnight sector at low solar flux level. The daytime wind is found to be generally more stable than the nighttime wind, particularly unresponsive to geomagnetic activities. Predictions from the Horizontal Wind Model find good agreement with the CHAMP-observed wind at high solar flux levels during nighttime. At low solar flux levels, however, the model strongly underestimates the westward wind during morning hours by 50–120 m s$^{-1}$ depending on season. The major difference between the HWM-predicted and the CHAMP-observed wind is seen in the phase of its diurnal variation. The CHAMP-observed wind turns eastward around 1200–1300 MLT instead of 1600–1700 MLT predicted by the model. Comparisons with ground FPI observations and the NCAR Thermosphere-Ionosphere-Electrodynamics General Circulation Model (TIEGCM) predictions show that the solar flux effect obtained from CHAMP is consistent with that modeled by TIEGCM. The solar flux dependence of zonal wind found here together with that of the zonal ion drift found in previous studies reflect the relative importance of the E- and F-region wind dynamo in the thermosphere-ionosphere coupling process. Furthermore, these wind measurements indicate that the Earth's atmosphere superrotates. The average superrotation speed amounts to about 22 m s$^{-1}$ for a solar flux level of $F10.7 \approx 100 \times 10^{-22}$ W m$^{-2}$ Hz$^{-1}$ but increases to 63 m s$^{-1}$ for $F10.7 \approx 190 \times 10^{-22}$ W m$^{-2}$ Hz$^{-1}$. Finally, the wind behavior presented in this study is longitudinally averaged and may differ from wind measurements at a certain longitude.

**Citation:** Liu, H., H. Lühr, S. Watanabe, W. Köhler, V. Henize, and P. Visser (2006), Zonal winds in the equatorial upper thermosphere: Decomposing the solar flux, geomagnetic activity, and seasonal dependencies, *J. Geophys. Res.*, *111*, A07307, doi:10.1029/2005JA011415.

## 1. Introduction

[2] Thermospheric neutral winds play an important role in the ionosphere-thermosphere coupling through dynamo effects and transportation of the plasma along the magnetic field lines [*Rishbeth*, 1972a; *Richmond et al.*, 1976; *Behnke et al.*, 1985; *Richmond and Roble*, 1987]. Measurements of neutral winds are made mainly using three types of techniques, namely, optical, incoherent scatter radar, and satellite drag. Optical technique, i.e., the Fabry-Perot Interferometer

[1]Division of Earth and Planetary Science, Hokkaido University, Sapporo, Japan.
[2]GeoForschungZentrum Potsdam, Potsdam, Germany.
[3]Department of Earth Observation and Space Systems, Delft University of Technology, Delft, Netherlands.


0148-0227/06/2005JA011415$09.00

(FPI), is recently most widely used, measuring the neutral wind through observations of the Doppler shift of airglow or auroral emissions (i.e., the 135.6 nm, 557.7 nm, or 630 nm emissions) at certain altitudes in the E or F region [*Bittencourt and Tinsley*, 1976; *Sipler et al.*, 1983; *Wharton et al.*, 1984; *Meriwether et al.*, 1986; *Burnside and Tepley*, 1989; *Biondi et al.*, 1990, 1999; *Coley et al.*, 1994; *Emmert et al.*, 2001]. Incoherent scatter radar provides estimations of the neutral wind by inferring it from the observed ion motion [*Balsley et al.*, 1976; *Emery*, 1978; *Brekke et al.*, 1994]. The satellite drag technique is probably the most ancient one, frequently used in the 1950s to 1970s in the form of orbital evolution analysis. This technique measures the wind through its effect on the satellite's orbital evolution or the direct acceleration/deceleration it causes on the satellite [*King-Hele*, 1964; *King-Hele and Walker*, 1983; *Marcos and Forbes*, 1985]. In principle, it can be used for measurements of winds at all altitudes. Each method has its technical limitations. The optical technique faces the uncertainty of the emission height and the zero-velocity line in addition to the restriction by sunlight. The physical assumptions used by the radar technique break down under disturbed conditions. The orbital analysis was criticized for lacking of time and spatial resolution, though it is theoretically free from physical complications associated with the first two techniques. However, acceleration analysis has greatly improved the resolution of the wind measurements obtained through satellite drag. At the same time, it keeps the virtue of being physically clean. However, surprisingly, only limited results of neutral winds from accelerometer analysis have been reported [*Marcos and Forbes*, 1985; *Forbes et al.*, 1993], in contrast to the large database of optical and radar observations. This limitation hinders us from uniting the advantages of different techniques for a better understanding of the neutral dynamics.

[3] The accelerometer on board the CHAMP satellite has been providing reliable and continuous measurements since August 2000. The use of simultaneous observations from global positioning system (GPS) has significantly improved the calibration of the CHAMP accelerometer; hence neutral wind and density can be reliably obtained from the nongravitational acceleration. As CHAMP is in a near-circular, polar orbit (87.3° inclination), with a precession rate of $\sim$1.5° per day, it provides a coverage of all local times and latitudes every 130 days. These long-period continuous measurements extend considerably the database of neutral winds obtained from accelerometers.

[4] Using these measurements, the present study endeavors to serve two purposes. One is to evaluate the empirical Horizontal Wind Model (HWM) [*Hedin et al.*, 1996, and references therein]. The other is to contribute needed information on the climatology of F-region wind which is still poorly specified by current models as shown in many studies [e.g., *Meriwether et al.*, 1986; *Fejer et al.*, 2002]. The climatological aspects examined here include the variation of zonal wind with season, solar flux, and geomagnetic activity levels in the equatorial upper thermosphere. Such variations during nighttime have been investigated considerably, owing to the large database of optical measurements [*Bittencourt and Tinsley*, 1976; *Sipler et al.*, 1983; *Meriwether et al.*, 1986; *Burnside and Tepley*, 1989; *Biondi et al.*, 1990; *Emmert et al.*, 2004]. Observations of daytime F-region zonal wind have been rather limited to the DE-2 satellite in the early 1980s [e.g., *Wharton et al.*, 1984; *Killeen et al.*, 1988] and UARS satellite in the 1990s [e.g., *Fejer et al.*, 2000; *Emmert et al.*, 2002]. However, most of these studies could not separate geomagnetic activity from solar flux level for different seasons due to insufficient data samples. Since these factors may simultaneously influence the wind, it is possible that results obtained from analysis without separating them may be inconclusive. The 3-year CHAMP observations with 24-hour local time coverage enable us to perform simultaneous separation of these conditions within one consistent data set. This augments previous studies and may stimulate a better understanding of the wind climatology.

[5] Furthermore, the diurnal variation of zonal winds under various conditions obtained here provides a straightforward estimation of the atmospheric superrotation and its variation with season, geomagnetic activity and solar flux level. We will therefore briefly comment on this legendary but nevertheless still controversial topic of atmospheric superrotation (see reviews of *Rishbeth* [2002] and *Gaposchkin* [2003]).

## 2. Methodology and Data Selection

### 2.1. Deriving the Neutral Wind and Density From Accelerometer Measurements

[6] In the work of *Liu et al.* [2005], we described how to retrieve the neutral mass density from accelerometer measurements. Here we make one step further to derive the neutral density and cross-track wind simultaneously. The atmospheric drag formula is read as

$$\vec{a} = -\frac{1}{2}\rho\frac{C_d}{m}A_{eff}V^2\vec{v}, \tag{1}$$

where $\vec{a}$ is the total acceleration due to air drag, $\rho$ is the total thermospheric mass density, $C_d$ is the drag coefficient, $A_{eff}$ is the effective cross-sectional area in the ram direction, $m$ is the satellite mass ($m$ = 520 kg for CHAMP), $V$ is the velocity of the satellite relative to the air, the ram direction $\vec{v}$ is the unit vector of this velocity. The coordinate system used in this study has its origin at the satellite's center of mass. The x-axis is aligned with the satellite's velocity vector along the nominal orbit, the z axis points downward and y is perpendicular to the orbital plane, completing the right-hand triad. This frame is often referred to as a Velocity-Nadir (VN) coordinate system. From formula (1) we readily deduce

$$\frac{V_y}{V_x} = -\frac{a_y}{a_x}. \tag{2}$$

Here $V_y$ is the total cross-track wind, which approximates the sum of the corotational wind ($V_c$ = 490 cos(*latitude*) m s$^{-1}$) and the zonal neutral wind ($U_{zonal}$) in the case of a polar orbiting satellite. Therefore

$$U_{zonal} = V_y - V_c = -\frac{a_y}{a_x}V_x - V_c \approx -\frac{a_y}{a_x}7.62\left(\text{km s}^{-1}\right) - V_c. \tag{3}$$

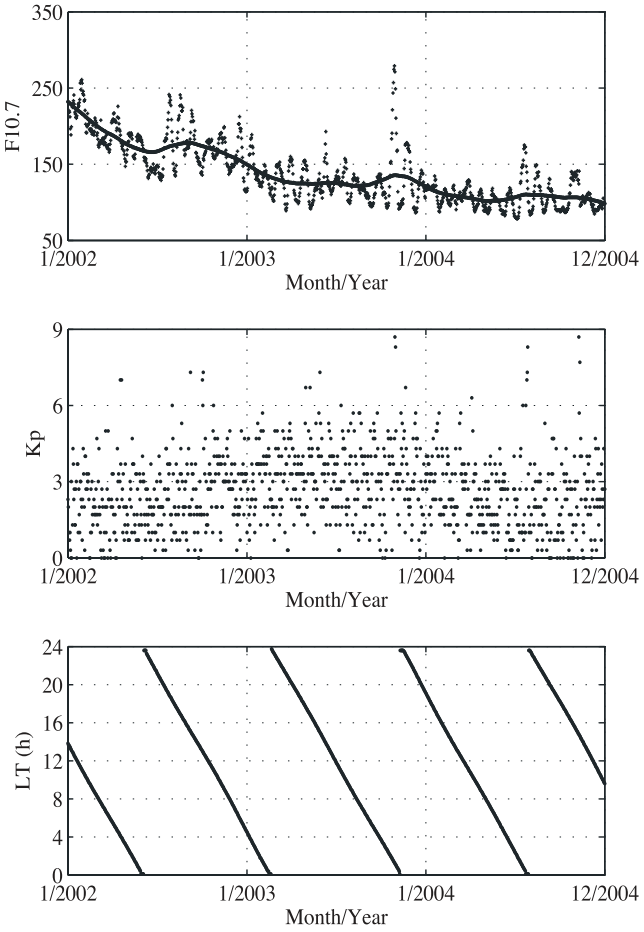


**Figure 1.** Variations of the solar flux proxy F10.7, the Kp index and the local time of the CHAMP satellite's ascending node during the period of Jan. 2002–Dec. 2004. The heavy line in the top panel shows the 81-day averaged F10.7 values. The F10.7 values are in unit of $10^{-22}$ W m$^{-2}$ Hz$^{-1}$.

Here $V_x$ is approximated with the satellite's flight velocity, and the meridional neutral wind is neglected. With the velocities obtained above, the total velocity $V$ and the neutral density are calculated using formulae (4) and (5) in the work of *Liu et al.* [2005]. The influence of the cross-track neutral wind is thus taken into account in the obtained thermospheric mass density. The difference between this method and the one first described by *Marcos and Forbes* [1985] is that we have utilized formula (2) to obtain the cross-track wind more straightforwardly than the iterative procedure they described. In this way, we can also effectively avoid influences from uncertainties in the satellite drag coefficient and the effective cross-sectional area on the wind calculation. We have compared these two different methods and found they yield very similar results. Neglecting the contribution of meridional wind in $V_x$ may cause an error in the obtained zonal wind but typically less than 3% in the equatorial region (given a meridional wind of $<200$ m s$^{-1}$). The fact that CHAMP's orbit (87.2° inclination) is not strictly polar in principle also causes an error. However, it is below 0.2% in the equatorial region. Given the accelerometer's precision of $3 \times 10^{-9}$ m s$^{-2}$, the obtained zonal wind from CHAMP has a precision of $\sim$20 m s$^{-1}$. In addition, it has a systematic error about 15 m s$^{-1}$ (see the error budget in Appendix A).

[7] Although the method described above is clear-cut, considerable work has to be done to the original accelerometer readings before this method can be applied. This includes removing other nongravitational forces (i.e., the solar radiation pressure), applying bias corrections and scale factors, and rotating the accelerometer measurements into the VN coordinates. Detailed descriptions for these procedures are given in Appendix A for further references. The application of these procedures takes care of major nongravity, nonair drag influences on the acceleration measurements and hence assures reliable wind and density measurements to be retrieved.

### 2.2. Data Selection and Processing

[8] We derive the neutral wind from the satellite drag measurements with a 10-s time resolution. Spurious spikes and accelerations related to attitude maneuvers are removed from these measurements. The data period covers from DOY 1/2002 to DOY 363/2004, in total 1093 days over 16,400 orbits. These measurements are grouped according to season, solar flux, and geomagnetic activity levels. Seasons are classified into three periods, namely, June solstice, equinoxes (combined), and December solstice, covering 90 days, 180 days, and 90 days, respectively, with centers at the corresponding solstices or equinoxes in each year. Two solar flux levels are defined as "low" for F10.7 $<$ 140, and "high" for F10.7 $\geq$ 140. Two activity levels are defined, with "quiet" for Kp $<$ 3, and "disturbed" for Kp $\geq$ 3. The variation of the F10.7, Kp index, and the local time of the satellite's ascending node during this period is shown in Figure 1. Data in each group are then binned and averaged over magnetic local time (MLT) and geomagnetic latitudes with a 1h $\times$ 1° (latitude) grid. The equatorial zonal wind is obtained by averaging the wind within a band of 5°S to 5°N geomagnetic latitudes. In order to clarify general trends, a 3-point running average was applied to remove high-frequency wind fluctuations. Since we fix simultaneously the season, solar flux level, and geomagnetic activity level for each data group, these three influencing factors are confidently separated from each other. In addition, Figure 2 shows that there are over 90 satellite passes in any local time bin for each group. This assures that the mean wind values represent typically observed values instead of extreme ones for each condition. The 24-hour coverage with ample sampling at each local time enables the possibility and ensures the statistical significance of results presented below.

[9] The Horizontal Wind Model (HWM), version 93, is used for comparison. To facilitate the closest comparison, model values were generated for each sample point of the measurements at both orbit and 400 km altitudes with the same solar radio flux (F10.7) and magnetic activity (Ap index) as those for the CHAMP measurements. These values were subsequently binned and averaged in the same way as that for the CHAMP measurements. Since the model values show little difference between 400 km and the orbit height (ranging from 365–460 during 2002–2004), we will present the values at 400 km altitude in the following sections.

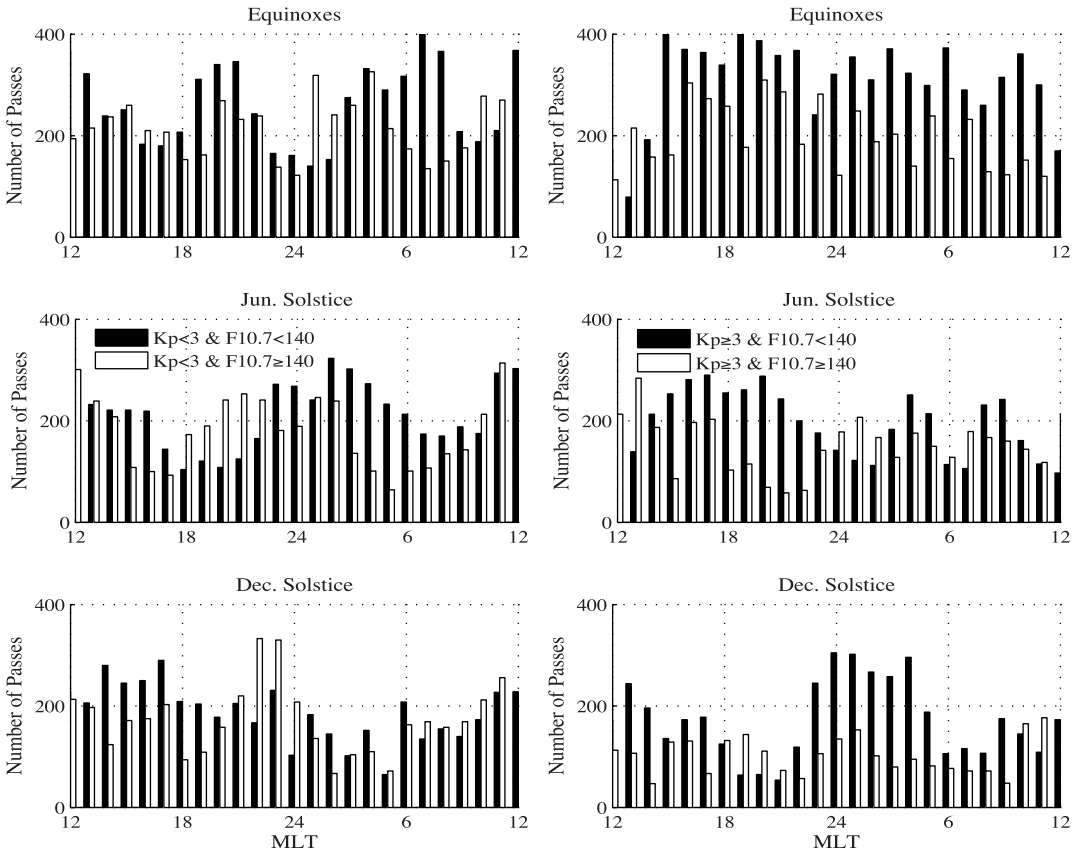


**Figure 2.** Number of satellite passes from CHAMP in each local time bin under various solar flux and geomagnetic activity conditions for each season. Equinoxes is a combined season of spring and autumn.

[10] Combined equinox is used here instead of separate ones. This is firstly because the current data set does not provide sufficient sample points for separate equinoxes, particularly at quiet geomagnetic conditions. Second, because both empirical models like HWM and numerical models like TIEGCM have shown rather small differences between the March and September equinoxes. Therefore the use of combined equinox may not severely compromise the characteristics of equinox winds presented below.

## 3. Equatorial Zonal Winds Observed By CHAMP

### 3.1. Average Diurnal Variation

[11] Figure 3 shows the zonal wind averaged over all seasons and all geomagnetic activity levels, but at two different solar flux levels. The low solar flux level ($F10.7 < 140$) corresponds to a mean F10.7 of ~100, while the high solar flux level ($F10.7 \geq 140$) corresponds to a mean value of ~190. The HWM model values are shown as gray curves for comparison. The standard deviation indicates the scattering of wind velocities in each corresponding local time bin. The model gives almost uniform scattering at all magnetic local times. However, CHAMP observes a diurnal variation of the standard deviation, with larger scattering at night than at day. This is consistent with the high variability of the nighttime wind, as also seen in FPI observations [e.g., *Burnside and Tepley*, 1989; *Biondi et al.*, 1990]. In the following sections, we will concentrate on features shown by the mean velocity of the wind.

[12] The equatorial zonal wind derived from CHAMP starts to blow eastward after 1200 MLT (see Figure 3). Up to 1800 MLT, there is no significant difference observed for different solar flux levels. A larger eastward wind is then observed at night for high F10.7 levels. The switch of the wind direction from eastward to westward occurs at 0600 MLT for high F10.7 and around 0300–0400 MLT for low F10.7 level. Peak westward winds are encountered

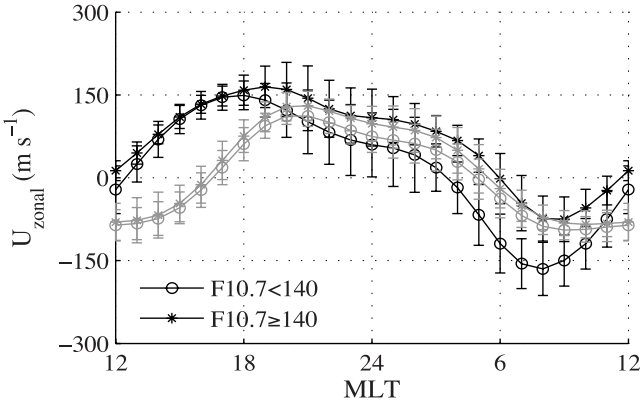


**Figure 3.** Average zonal wind over all seasons and all geomagnetic activity levels but for two different solar flux levels. Black curves represent CHAMP observations and gray ones HWM predictions. Positive means eastward. The wind is averaged within 5°S–5°N geomagnetic latitudes.

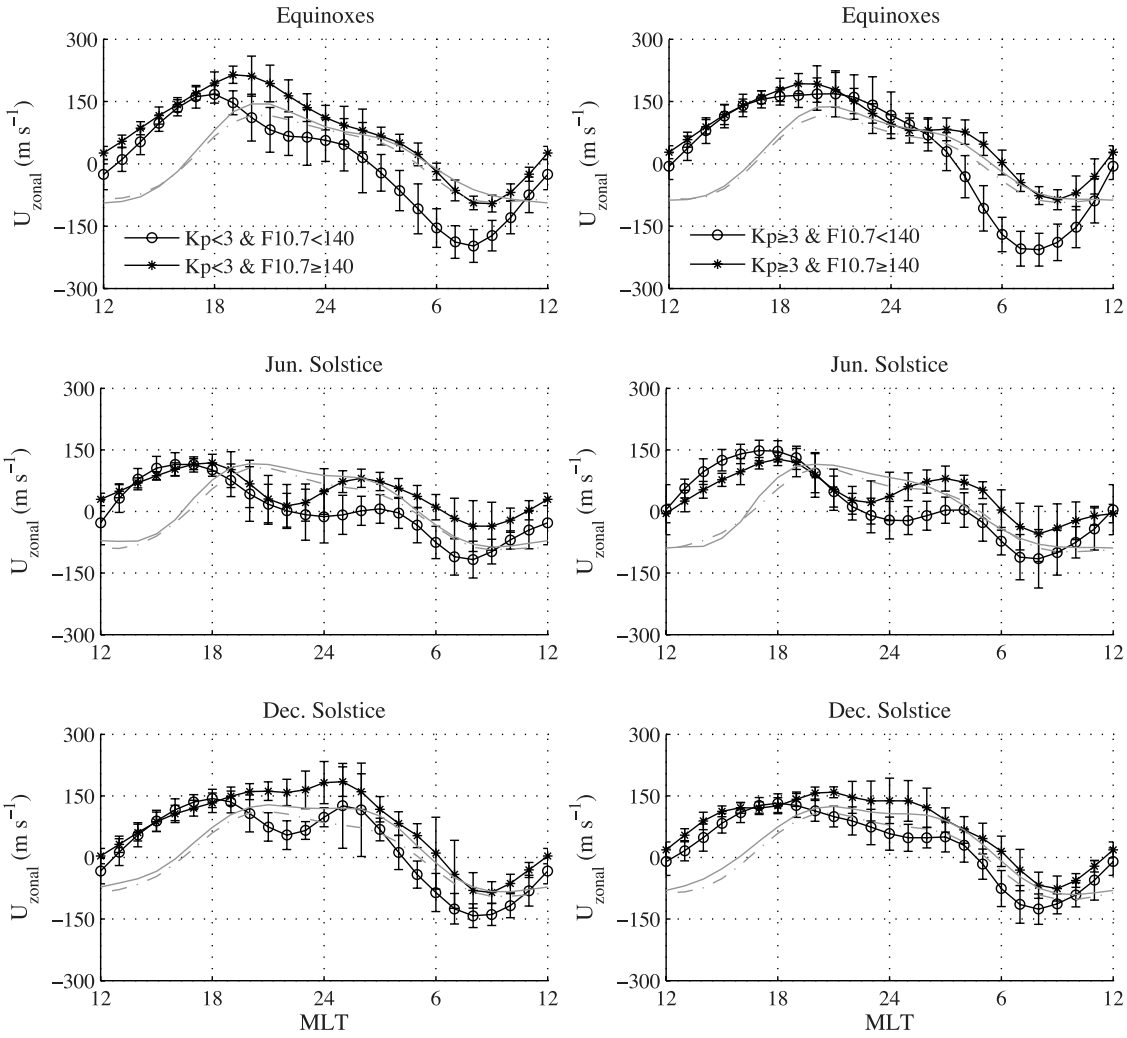


**Figure 4.** Zonal wind at about 400 km altitude in different seasons at two different solar flux levels. Positive means eastward. The left column is for quiet and the right one for disturbed geomagnetic conditions. Black curves represent CHAMP observations. Gray curves represent HWM predictions, with the solid curve for F10.7 $\geq$ 140 and the dashed one for F10.7 < 140 under corresponding geomagnetic conditions.

in the prenoon sector around 08 MLT for both solar flux levels. However, the speed at low F10.7 level is almost double of that observed at high F10.7 level ($-90$ m s$^{-1}$ for mean $F10.7 \approx 190$ and $-180$ m s$^{-1}$ for mean $F10.7 \approx 100$).

[13] The HWM model values closely resemble the CHAMP measurements over a large MLT range. This is particularly true at high solar flux levels between 2100 and 1000 MLT. For times of low solar flux level, good agreement can only be claimed between 2000 and 0200 MLT. During morning hours, the prevailing westward wind is strongly underestimated by HWM at low F10.7 levels. A major discrepancy is seen in the postnoon sector, where the observed wind turns eastward around 1200–1300 MLT instead of around 1600–1700 MLT predicted by the model. This leads to a phase difference of $\sim$4 hours between the diurnal variation obtained from HWM and CHAMP.

[14] In the following, we examine various influences on this average diurnal curve from solar flux, geomagnetic activity, and season.

### 3.2. Influences of the Solar Flux

[15] Zonal winds at different solar flux levels are shown in Figure 4 for different seasons. Panels in the left column are for quiet-time wind (mean Kp $\approx$ 2.0), and the ones on the right for disturbed-time wind (mean Kp $\approx$ 4.3). The dashed and solid gray lines represent model values at low (mean F10.7 $\approx$ 100) and high (mean F10.7 $\approx$ 190) solar flux levels, respectively. Since the corresponding standard deviation for HWM is similar to that shown in Figure 3, it is omitted here to facilitate the comparison between various curves. Influences of solar flux levels on quiet- and disturbed-time zonal winds can be summarized as follows.

[16] For quiet-time wind around equinoxes, the elevation of the solar flux produces an eastward difference wind of 50–110 m s$^{-1}$ during 1900–1000 MLT. This leads to a stronger nighttime eastward wind and a weaker daytime westward wind at high solar flux level. In addition, the east-to-west turning of the wind direction at high solar flux level occurs around 0400–0500 MLT instead of 0100 MLT at

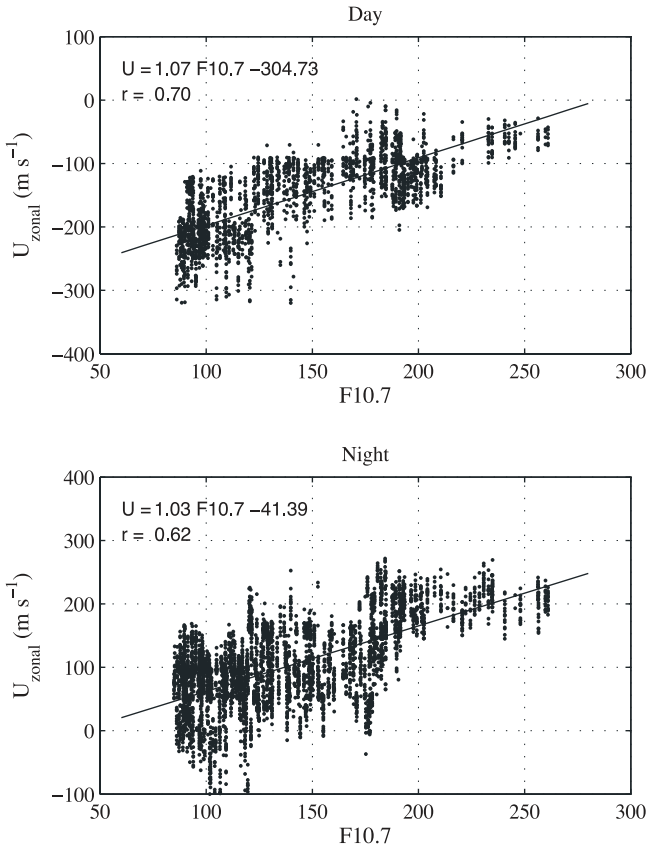


**Figure 5.** Distribution of the peak wind velocity versus F10.7 in the equatorial region, for day and night side respectively. Positive means eastward. With increasing solar flux F10.7, the peak westward wind becomes weaker and the peak eastward wind grows stronger.

low solar flux level. The solar flux effect between 1200 and 1800 MLT appears to be rather insignificant. Around June solstice, the influence is mainly seen on the dawnside (2400–1200 MLT), with an eastward difference wind between high and low solar flux levels. Strong eastward winds with velocity of ~100 m s$^{-1}$ are observed in the postmidnight sector at high solar flux level, in comparison to a nearly zero wind at low solar flux level. The morningtime westward wind is weakened at high solar flux level. Around December solstice, increasing the solar flux produces an eastward difference wind during 2000–1100 MLT. The enhancement of the premidnight eastward wind is particularly strong, reaching over 100 m s$^{-1}$ around 2200 MLT. The solar flux effect under disturbed conditions (right column of Figure 4) is similar to that under quiet conditions. The only exception occurs during 1900–0200 MLT around equinoxes, where increasing the solar flux level produces little effect on the wind in comparison to a strong enhancement about 100 m s$^{-1}$ shown in the panel on the left.

[17] The HWM model exhibits an eastward difference wind produced by the elevation of the solar flux level, particularly at night. However, its magnitude is below one third of that shown in the CHAMP observations, as indicated by the displacement between different F10.7 curves for two data sets. Furthermore, the modeled effect seems to vary little with season and geomagnetic activity.

[18] To examine the trend of wind velocity with increasing solar flux in some detail, we have carried out a correlation analysis of the peak wind velocity with the F10.7 value. The results are shown in Figure 5, for the dayside and nightside separately. It is evident that the average peak westward (eastward) wind speed shows a rough negative (positive) dependence on the F10.7 values.

### 3.3. Influences of the Geomagnetic Activity

[19] Figure 6 demonstrates that the influences of geomagnetic activity on zonal winds depend on season and solar flux level. The mean Kp value is ~2.0 for $Kp < 3$ and ~4.3 for $Kp \geq 3$. Around equinoxes, increasing geomagnetic activity enhances the nighttime wind by over 50 m s$^{-1}$ at low solar flux levels but produces little effect at high solar flux level. Around June solstice, the wind appears rather unresponsive to geomagnetic activities except for a slight enhancement around 1800 MLT at low F10.7 level. Around December solstice, increasing geomagnetic activity weakens the wind in the postmidnight sector by about 40 m s$^{-1}$ regardless of solar flux levels. The HWM model shows a very slight reduction ($\leq$10 m s$^{-1}$) of the nighttime wind in all seasons produced by increasing geomagnetic activity.

[20] In comparison with Figure 4, the magnitude of the geomagnetic activity effect revealed here is less than half of the solar flux effect (as indicated in the displacement between two curves in each panel). Furthermore, this effect is mainly observed on the nightside. This indicates that statistically studying the geomagnetic effect without sorting the measurements with solar flux level will likely lead to inaccurate conclusions on both dayside and nightside winds. Studying the solar flux effect without distinguishing different geomagnetic conditions would lead to similar problems for the nightside wind, though it seems less problematic for the dayside wind.

### 3.4. Seasonal Variations

[21] Both the temporal variation and magnitude of the wind vary with season. Owing to strong solar flux influences on the wind mentioned above, its seasonal variation also depends on solar flux level as clearly shown in Figure 6. At low solar flux level around equinox, the maximum eastward (~150 m s$^{-1}$) and westward winds (~−200 m s$^{-1}$) are encountered around 1800 MLT and 0800 MLT, respectively. The wind direction switches from eastward to westward around 0300–0400 MLT. The wind around June solstice differs largely from the equinox wind around midnight. Instead of blowing eastward at a speed over 80 m s$^{-1}$, it decreases to nearly zero during 2100–0300 MLT. Around December solstice, the wind again blows eastward throughout the night as around equinoxes but decreases less rapidly toward dawn. The daytime westward wind exhibits similar local time variation in all seasons. The seasonal variation changes considerably at high solar flux level. The westward turning of the wind direction in the early morning generally occurs 2 hours later. The most prominent feature is a double-hump structure at night around June solstice, with strong eastward wind over 100 m s$^{-1}$ around 1800 MLT and 0100 MLT, weak wind below 30 m s$^{-1}$ near midnight. This structure was reported in previous studies [e.g., *Meriwether*

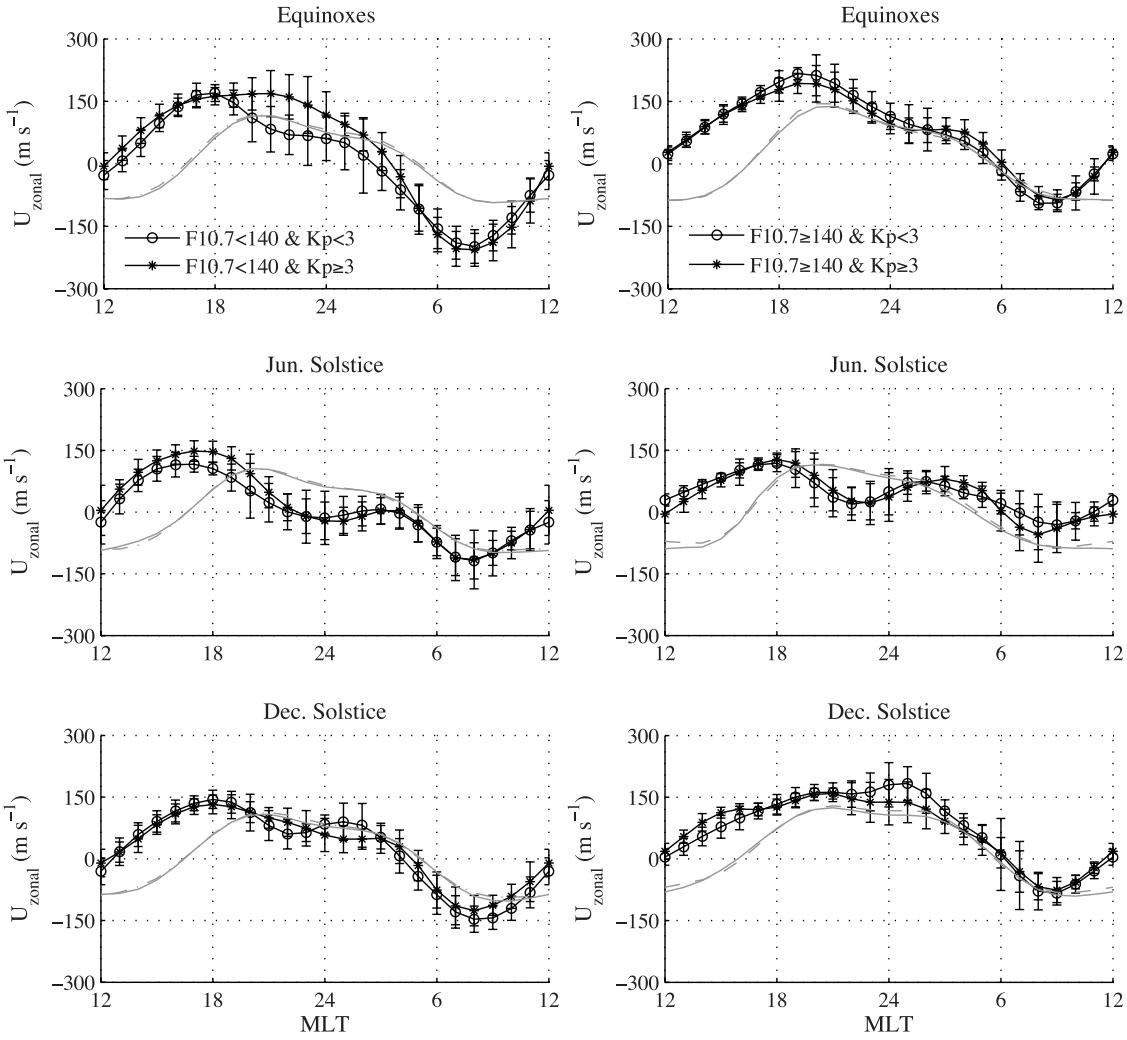


**Figure 6.** Zonal wind at about 400 km altitude in different seasons at two different geomagnetic activity levels. The left column is for F10.7 < 140 and the right one for F10.7 $\geq$ 140 conditions. Black curves represent CHAMP observations. Gray curves represent HWM predictions, with the solid curve for Kp $\geq$ 3 and the dashed one for Kp < 3 at corresponding solar flux levels.

*et al.*, 1986; *Herrero et al.*, 1985; *Biondi et al.*, 1990]. Our study seems to indicate that it is prominent at high solar flux levels regardless of geomagnetic activity level. A rather stable feature in the seasonal variation is that the average wind velocities (both eastward and westward) are about 30% smaller around June solstice than in other seasons regardless of solar flux or geomagnetic activity levels.

[22] The HWM model shows little seasonal variation, particularly at low solar flux level. Furthermore, the model prediction of nighttime wind deviates significantly from the CHAMP observation around June solstice.

## 4. Discussion

[23] The above CHAMP measurements represent a large data set of continuous observation of the upper thermospheric zonal wind on both dayside and nightside. The considered time interval of 2002–2004 is characterized by major changes of the solar flux level associated with the declining phase of the solar cycle. The F10.7 value dropped from 250 to 78 as seen in Figure 1. These observations have revealed a strong solar flux influence on both daytime and nighttime wind. It overrides the geomagnetic activity effect, which is found to be limited to the nightside.

[24] In the following, we will first discuss discrepancies between the CHAMP-observed winds and the one predicted by the HWM model. We then compare our results on the solar flux effect with those obtained from ground FPI observations and from the TIEGCM model simulations presented by *Biondi et al.* [1999]. The role of atmospheric pressure gradient in driving the zonal wind is also investigated. Finally, we comment on indications of the atmospheric superrotation from CHAMP measurements.

### 4.1. Comparisons Between CHAMP and HWM

[25] On average the CHAMP-observed wind agrees very well with the predictions of the HWM model for high F10.7 levels and during night hours as seen in Figure 3. This favorable comparison lends confidence on both CHAMP measurements and the HWM model prediction under these conditions. Significant differences have been found at low solar flux levels and also on the dayside, which may arise

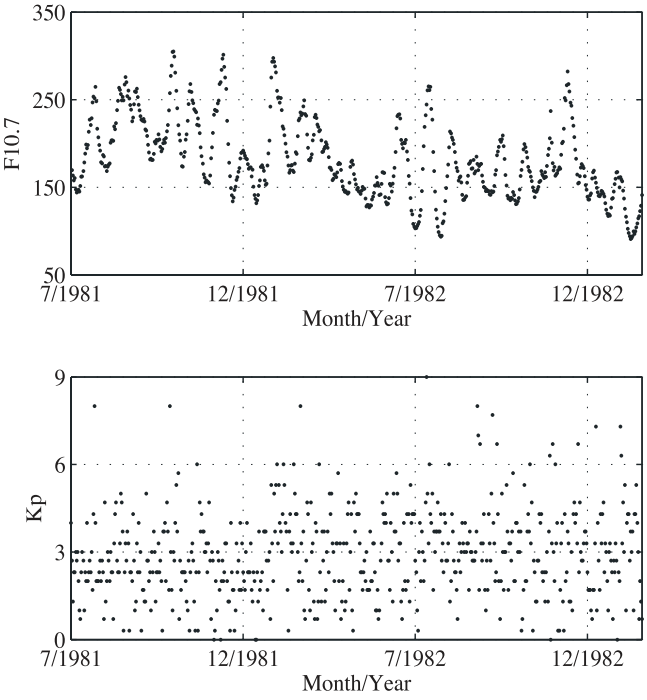


**Figure 7.** Variations of the solar flux (F10.7) and the Kp index during the DE-2 period of Jul. 1981–Feb. 1983.

from the limitation of the data sets used by the HWM model as discussed below.

[26] The HWM is an empirical model which integrates various data of neutral wind observations. However, these data form a complementary rather than an overlapping set in space and time. For instance in the equatorial region, two ground FPI stations (Arecibo and Arequipa) and one IS radar station (Arecibo) contributed to wind measurements below 350 km at night. While above 350 km, observations came from AE-E and DE-2 satellites, with AE-E and DE-2's FPI measurements contributing to the meridional and DE-2's WATS measurements contributing to the zonal component of the wind [*Hedin et al.*, 1991]. Therefore, though they may be indirectly supplemented by FPI and IS observations at night, HWM predictions for zonal wind at 400 km are largely based on DE-2's WATS measurements. The DE-2 data set covers periods from August 1981 to February 1983. Wind derived from the DE-2 satellite has been reported in many studies [*Wharton et al.*, 1984; *Coley et al.*, 1994; *Wu et al.*, 1994]. Since almost 90% of DE-2 measurements were made under $F10.7 \geq 140$ conditions (see Figure 7), the model values are likely less representative for low solar flux levels. This would apparently lead to the large difference seen between HWM and CHAMP at low F10.7 level. Furthermore, since the ascending node of the DE-2 satellite traverses all local times in about one year, the wind obtained from the relatively short period of August 1981 to February 1983 suffers strongly from the locking between local time and season. The midnight/noon sectors were rarely sampled around solstices, hence contributing to noticeably larger deviations of HWM from CHAMP observations at night during these seasons. The relatively better agreement during December solstice may be owing to the FPI measurements at Arequipa used in HWM model, which was mainly available during local summer.

[27] The major difference between the HWM-predicted and the CHAMP-observed wind is seen in the phase of its diurnal variation. The CHAMP-observed wind turns eastward around 1200–1300 MLT instead of 1600–1700 MLT predicted by the model (see Figure 3). This leads to large differences on the dayside as noticed before. Neglecting meridional wind causes an error less than 3% in the CHAMP-observed winds and is unlikely to shift the time of its zero crossing by 3 hours. In particular, this velocity reversal occurs almost uniquely around 1200–1300 MLT in all seasons under all conditions, hence lending further confidence to the method we use. Several sources can be identified which may bias the DE-2 measurements, hence the HWM prediction on the dayside. First, the locking of local time and season mentioned above. It means that the curve of the wind diurnal variation portrayed by DE-2 is a patched one, with parts of the curve representing solstice, and other part representing equinoxes conditions. Second, the altitude of DE-2 measurements ranges from 200 to 700 km [*Wharton et al.*, 1984]. In spite of being a much larger data set, CHAMP measurements are collected within a much smaller altitude range between 365 and 460 km. Although the neutral wind is generally assumed to be almost constant throughout the F region, there have rarely been direct observations to confirm this on either the magnitude or the phase of its diurnal variation. On the contrary, *Fejer et al.* [1981] has pointed out that the reversal time of the zonal plasma drift varies with altitudes between 275 and 500 km. Given the close coupling between the neutral and plasma motions, it is possible that averaging wind measurements over altitudes between 200 and 700 km causes apparent smearing of the reversal time at different altitudes. Finally, techniques used by DE-2 and CHAMP for wind measurements are completely different. The DE-2 satellite uses a spectrometer [*Spencer et al.*, 1981], while the CHAMP satellite uses an accelerometer. Discrepancies arising from different instruments cannot be ruled out.

[28] Interestingly, the temporal variation of the wind obtained from CHAMP closely resembles that of the ion drift deduced from the vector electric field instrument (VEFI) on board DE-2. This contrasts to the similarity found between the DE-2-derived wind and the ion drift seen by the ion drift meter (IDM) also on board DE-2. Using VEFI measurements, *Maynard et al.* [1988] have found in the zonal ion drift a stable reversal time around 1200 MLT and a variable reversal time between 0400 and 0600 MLT [see *Maynard et al.*, 1988, Figure 8]. This fits surprisingly well with our observations of the neutral wind. No clear reason has been published to explain the discrepancy between the zonal ion drift measured by IDM and VEFI on board the same spacecraft. Apparently, more observations of the F-region wind on the dayside are necessary to explain the discrepancy between the CHAMP and DE-2 measurements.

### 4.2. Comparison of Solar Flux Effects Seen By CHAMP, Ground FPI, and TIEGCM

[29] Using ground FPI measurements, *Biondi et al.* [1999] studied the solar flux effect on the equatorial nighttime wind between 255 and 285 km altitude in

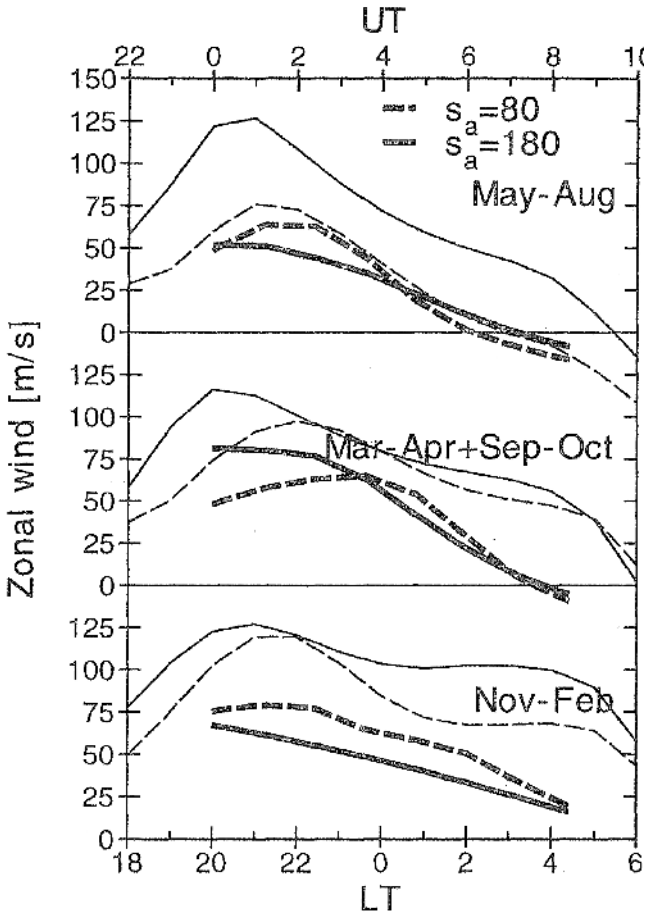


**Figure 8.** Zonal wind around 255–285 km altitude for Kp $\leq$ 3 as observed by ground FPI at Arecibo and predicted by TIEGCM. Heavy lines: FPI observations; Light lines: TIEGCM predictions. See text for more detail. (reprinted from *Biondi et al.* [1999]).

different seasons under quiet geomagnetic conditions. The FPI data set they use is larger than the corresponding Arecibo and Arequipa measurements used in the HWM model. Furthermore, *Hedin et al.* [1991] pointed out that "the F10.7 trend in HWM model is largely the result of differences between different data sets taken at different parts of the solar cycle" and "the importance of having a long series of data from a given instrument can hardly be overestimated in the analysis of solar activity variations." Therefore we believe that the solar flux effects obtained by *Biondi et al.* [1999] and our current study are likely more accurate than the one predicted by the HWM model. In addition, *Biondi et al.* [1999] also presented TIEGCM simulation results on the solar flux dependence of the quiet-time F-region wind at night. In the following, we compare their results shown in Figure 8 and our results shown in the left column of Figure 4 between 1800 and 0600 MLT.

[30] Around equinoxes, both CHAMP measurements and the TIEGCM predictions (second panel of Figure 8) show an enhancement of the wind at high solar flux levels throughout the night, in comparison to a premidnight enhancement and a postmidnight reduction shown in the FPI observations. In addition, the temporal variation seen by CHAMP at high solar flux levels closely resembles the model predictions, with maximum wind around 2000 MLT and the westward turning around 0600 MLT. Around June solstice, all three sets of data show wind enhancement with increasing solar flux in the postmidnight sector. However, differences exist in the premidnight sector. Around December solstice, both CHAMP and TIEGCM reveal a positive dependence of the wind on solar flux levels at night, opposite to the negative dependence shown in the FPI measurements (bottom panel of Figure 8). Therefore we conclude that the solar flux effect obtained from CHAMP agrees fairly well with the TIEGCM simulations but rather differs from the ground FPI measurements. The difference seen in the magnitude of the wind velocity may be partly due to the altitude difference between CHAMP ($\sim$400 km) and FPI/TIEGCM ($\sim$255–285 km). Longitudinal variation of the wind could also play an important role, particularly in producing the large differences between CHAMP/TIEGCM and the FPI observations. With the relatively large magnetic declination angle ($-10^\circ$), it is possible that the wind behavior at this FPI site could deviate significantly from the longitudinally averaged one, which is the case for the CHAMP-derived wind presented in this study.

[31] It may be interesting to compare the solar flux dependence of zonal wind obtained here with that of the zonal plasma drift. The zonal wind, as observed from CHAMP, tends to grow stronger with increasing solar flux level at night but becomes weaker with it at day (see Figure 5). In comparison, the nighttime eastward plasma drift has also been found to increase at higher solar flux levels, but the westward drift at day varies little with solar flux levels [*Fejer et al.*, 1991]. The relative behavior of the neutral and plasma motion is consistent with the relative importance of the E- and F-region dynamo in generating ionospheric electric fields at low latitudes [e.g., *Kelley*, 1989]. On the nightside, the F-region dynamo dominates, and the local thermospheric wind drives the electrical system hence the F-region plasma motion. This leads to similar solar flux dependence of the neutral and plasma zonal drift at night. On the dayside, the E-region dynamo dominates, and the zonal plasma drift is primarily driven by winds in the E region. Since the E- and F-region winds behave quite differently, it is not surprising to see different trend of the F-region neutral and plasma motion during day. Furthermore, *Cho and Yeh* [1970] pointed out that with increasing solar flux level, the ion drag increases more rapidly than the pressure-gradient force on the dayside. This leads to a weaker westward wind, just as CHAMP observed.

[32] Another prominent feature of the solar flux found in this study is that it strongly influences both the daytime and nighttime wind. It overrides the geomagnetic effect, which is found to be limited to the nightside. This may not appear to be surprising given the following explanation. In this study, the solar F10.7 flux level is used as a rough indication for the solar EUV radiation level. The solar EUV radiation directly heats and ionizes the equatorial neutral atmosphere to produce day-night pressure gradient and ion drag. In comparison, the geomagnetic activity represented by the Kp index is mainly related to the solar wind intensity and the orientation of the interplanetary magnetic field (IMF) em-

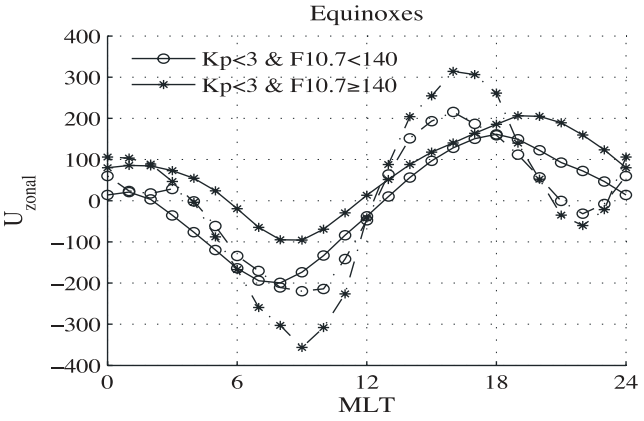


**Figure 9.** Neutral wind around equinoxes. Solid curves represent observed wind, and dashed curves represent estimated wind without ion-drag term.

bedded in it. Its effects on equatorial winds generally originate from high latitudes, evolving more complicated ionosphere-thermophere coupling processes via ion drag, global wind circulation, wind dynamo, etc. [*Blanc and Richmond*, 1980; *Richmond and Roble*, 1987]. The propagation of the disturbance from high to low latitudes is found to be better facilitated on the nightside, where the ion drag is smaller [*Fuller-Rowell et al.*, 1994, 1996]. In addition, attenuation of the disturbance often occurs during the propagation. On the basis of these modeling results, it is not surprising that effects of moderate geomagnetic activity shown in this study is mainly limited to the nightside equatorial region, with relatively small magnitudes.

### 4.3. Role of Pressure Gradient in Driving the Equatorial Zonal Wind

[33] In the equatorial upper thermosphere, the atmospheric pressure gradient is generally known as the primary driver of the neutral wind. The ion drag is an important impeding force, which regulates the neutral wind considerably. The DE-2 observations of the ion and neutral drift have drawn much attention and also greatly advanced our understanding towards the ion-drag effect on neutral winds [e.g., *Coley et al.*, 1994]. In contrast, the role of pressure gradient as the principle driver has lacked sufficient investigation using in situ measurements. In this section, we attempt such an investigation using simultaneous measurements of total neutral mass density and wind from the CHAMP satellite.

[34] According to *Rishbeth* [1972b], the momentum equation governing the equatorial zonal wind $U_x$ in the upper thermosphere can be expressed as

$$\rho \frac{dU_x}{dt} = -\frac{\partial p}{\partial x} - n_i m_i \nu_{in}(U_x - V_{ix}) + \mu \frac{\partial^2 U_x}{\partial z^2}. \quad (4)$$

Here $p$ is the neutral air pressure, $n_i$ and $m_i$ are the number density and mass of the ion, $\nu_{in}$ is the ion-neutral collision frequency, $V_{ix}$ is the zonal ion drift, and $\mu$ is the viscosity coefficient. Three terms on the right-hand side represent the air pressure gradient, the ion drag, and the viscosity, respectively. The viscosity term can be expressed as $\frac{\mu}{H^2}U_x$, where $H$ is the atmospheric scale height. The value $\mu$ is calculated as

$$\mu = 4.5 \times 10^{-5}\left(\frac{T}{1000}\right)^{0.71}. \quad (5)$$

Here $T$ is the neutral temperature. For the treatment of the average zonal wind, the temporal variation of the velocity and the inertial term at a certain point may be neglected in comparison to the much larger (by over ten times) pressure gradient there. This leads to $\frac{dU_x}{dt} \approx 0$. Therefore we have

$$\frac{\partial p}{\partial x} \approx -n_i m_i \nu_{in}(U_x - V_{ix}) + \frac{\mu}{H^2}U_x. \quad (6)$$

Since

$$p = nkT = \frac{k}{m}\rho T, \quad (7)$$

the zonal component of the pressure gradient can be expressed as

$$\frac{\partial p}{\partial x} = \frac{k}{m}\left(\frac{\partial \rho}{\partial x}T + \frac{\partial T}{\partial x}\rho\right). \quad (8)$$

Here $m$ is the average mass of the neutral particles and $k$ is the Boltzmann constant. The first term $\frac{\partial \rho}{\partial x}T$ is on average more than 5 times larger than the second term $\frac{\partial T}{\partial x}\rho$; thus the atmospheric pressure gradient is mainly determined by the density gradient and the neutral temperature.

[35] Since we do not have the simultaneous observations of ion drift, it is difficult to quantitatively examine the wind behavior using formula (6). However, we can neglect the ion drag term and roughly estimate a wind driven only by the pressure gradient. Taking direct measurements of $\rho$ from CHAMP and T from MSIS model, we can calculate $H$, $\mu$, and the pressure gradient. The obtained wind is shown in Figure 9 as dashed curves, along with the measured zonal wind for equinox quiet conditions at two different solar flux levels. Although this rough estimation cannot directly explain the wind variation with solar flux level, it shows two interesting features as pointed out below.

[36] First, it is evident that the temporal variation of the calculated wind tracks fairly well the observed one except in the premidnight sector. In particular, the occurring time of the direction switch around noon overlaps each other, indicating that the vanishing zonal wind around 1200–1300 MLT observed by CHAMP is consistent with the pressure gradient. This provides additional supporting evidence for the phase of the wind diurnal variation observed by CHAMP. Second, the pressure-driven wind is much larger than the observed wind on the dayside, hence demonstrating the important role of ion drag in slowing down the wind during day. At night, particularly in the premidnight sector, however, the estimated wind is smaller than the observed one. This suggests that the pressure gradient is insufficient to produce the observed wind, and other drivers are needed in this local time sector. This may first come from a positive ion drag relating to fast moving ions, driven either by additional polarization electric field

**Table 1.** Atmospheric Superrotation at 400 km Altitude at Equator

| | Equinoxes, m s$^{-1}$ | Jun Solstice, m s$^{-1}$ | Dec Solstice, m s$^{-1}$ | Average, m s$^{-1}$ |
|---|---|---|---|---|
| F10.7 < 140 | 22 | 11 | 33 | 22 |
| F10.7 $\geq$ 140 | 72 | 40 | 76 | 63 |
| F10.7 < 140 Kp < 3 | 11 | 11 | 37 | 20 |
| F10.7 < 140 Kp $\geq$ 3 | 30 | 19 | 30 | 28 |

[*Coley et al.*, 1994] or by penetration electric field from high latitude during disturbed time [*Fejer et al.*, 1979]. It may also come from tides propagated from the lower atmosphere [*Fesen*, 1996; *Meriwether et al.*, 1997]. How they could drive the wind is a separate question.

### 4.4. Atmospheric Superrotation

[37] Table 1 shows that the 24-hour averaged net wind velocity is eastward (positive) in all seasons under various geomagnetic and solar flux conditions, thus supporting the statement that the Earth's atmosphere superrotates [*King-Hele*, 1964]. One feature emerging from this table is the seasonal variation of the superrotational speed. It is higher around December solstice than around June solstice regardless of geomagnetic and solar flux levels. This seasonal variation agrees well with the result from satellite orbital analysis (see review of *King-Hele and Walker* [1983]). Effects of moderate geomagnetic activity are mainly seen at low solar flux levels, and they vary considerably with season.

[38] The most prominent feature revealed by this table is that the superrotational speed increases with increasing solar flux in all seasons. This is readily understood because an increase in solar flux generally reduces the westward wind and enhances the eastward, as shown in previous sections. The average superrotation is $\sim$22 m s$^{-1}$ at low solar flux level but reaching $\sim$63 m s$^{-1}$ at high solar flux level. This leads to a superrotation of $\sim$43 m s$^{-1}$ averaged over all conditions. Even taking into account the systematic error of 15 m s$^{-1}$, these values are smaller than the $\sim$100 m s$^{-1}$ obtained from satellite orbital analysis [*King-Hele and Walker*, 1983] and are larger than the 20 m s$^{-1}$ estimation from DE-2 satellite at high solar flux level [*Wharton et al.*, 1984]. However, they are rather close to the value of 47 m s$^{-1}$ given by a newer calculation based on the TIEGCM 2000 model [see *Rishbeth*, 2002, Table 1].

## Appendix A: Preprocessing the CHAMP Accelerometer Data

[39] High-accuracy accelerometer measurements can in principle be used for deriving the air mass density and neutral wind without physical complications. However, the raw accelerometer readings need to be carefully preprocessed. This procedure includes three major steps, namely, removing other nongravitational forces (i.e., the solar radiation pressure), corrections using bias and scale factors, and rotation of the accelerometer measurements into a suitable coordinate system.

[40] Readings of the accelerometer are not only influenced by air drag. For example, attitude maneuvers generate short-lived ($\sim$1 s) impulses. As part of the CHAMP data preprocessing, readings affected by attitude pulses or electric interferences are removed before decimating the 1 Hz sampling to 0.1 Hz [*Förste and Choi*, 2004]. This assures that the signal power of these disturbances does not enter the 10-s resolution data. Another nongravitational force acting on the satellite is the light pressure, mainly from the Sun and the Earth. Radiation from the Earth affects only the vertical acceleration component, $a_z$, which has not been taken into account. The solar radiation pressure influences all directions. The acceleration it asserts on the spacecraft can be expressed as

$$\vec{a}_s = f_s \kappa \frac{\vec{A} \cdot \vec{s}}{m} \vec{s}, \tag{A1}$$

where $\kappa = 4.56 \times 10^{-6}$ Nm$^{-2}$ is the solar radiation pressure constant, $m$ is the mass of the satellite, $\vec{a}$ is the surface area in normal directions, $\vec{s}$ is the Sun-pointing unit vector, and $f_s$ is a scaling factor depending on the optical properties of the surface. In our study, $f_s$ was determined experimentally from the jumps in acceleration at the times of the Sun terminator crossings. Maximum accelerations in the along-track direction are $18 \times 10^{-9}$ m s$^{-2}$ occurring in a noon/midnight orbit, and in cross-track direction they amount to $76 \times 10^{-9}$ m s$^{-2}$ in the dawn/dusk orbit. The uncertainty in the estimated values is about 3%, causing a systematic error of about 7 m s$^{-1}$ in the wind near the terminator (see Table A1).

[41] The accelerometer is an instrument which for CHAMP was unable to be calibrated to sufficient precision on ground. Bias and scale factors have thus to be determined in orbit. For this study the estimation of bias and scale factor for the along-track and cross-track axes of the accelerometer was integrated in an orbit determination from GPS satellite-to-satellite tracking (SST) observations. A state-of-art, high-degree, and high-order gravity field model, GGM01S, was used to distinguish between gravitational and nongravitational accelerations [*Tapley et al.*, 2004]. The bias and scale factor are determined in such a way that the sum of the accelerations from the corrected accelerometer observations and the other modeled/estimated accelerations (including those predicted by GGM01S) match best with the orbit derived from the GPS SST observations. This method has been described in detail by *Visser and van den IJssel* [2003]. Daily bias and scale factor were estimated for the time period ranging from DOY 140/2001 to 363/2004. The bias values for the cross-track axis displayed small drifts of about $2.5 \times 10^{-8}$ m s$^{-2}$ per year. The uncertainty in the bias estimation is about $3 \times 10^{-9}$ m s$^{-2}$. This uncertainty for the

**Table A1.** Error Budge for the Wind Derivation

| | | Error in Velocity, m s$^{-1}$ | |
|---|---|---|---|
| | Uncertainty | Random | Systematic |
| Solar radiation pressure[a] | 3% | - | 7 |
| Attitude | 0.02° | 2 | - |
| Scale factor | 3% | - | 15 |
| Bias | $3 \times 10^{-9}$ m s$^{-2}$ | 20 | - |
| Total | | 20 | 15[b] |

[a]This effect is mainly occurring near the terminator.
[b]This increases to 22 m s$^{-1}$ near the terminator.

cross-track acceleration actually do not affect the average cross-track wind, when derived from an even distribution of ascending and descending orbit arcs. This is because the resulting velocity errors have opposite signs for northbound and southbound tracks. It will, however, cause a random error (or noise) in the wind values within a local time bin. The scale factor has an uncertainty of 3%, leading to a systematic error about 15 m $s^{-1}$ in the wind velocity.

[42] For the derivation of the thermospheric wind from the accelerometer measurements, we use a coordinate system which has its origin in the center of mass of the satellite. The x axis is aligned with the velocity vector along the nominal orbit, the z axis points downward and y is perpendicular to the orbital plane, completing the right-hand triad. This system is often referred to as a Velocity-Nadir (VN) coordinate system. CHAMP is an Earth-oriented, three-axes stabilized spacecraft. The attitude is kept stable in the VN frame within a band of 2° about all axes. The uncertainty in the attitude measurement is below 0.02°, leading to a random error of 2 m $s^{-1}$ in the wind. Since the original three components of acceleration readings are done in the ACC coordinates, a transform into the VN frame has to be applied. This is done by three consecutive rotations

$$\vec{a} = R_x(-\alpha)R_y(-\beta)R_z(-\gamma)\vec{a'}, \tag{A2}$$

where $\vec{a'}$ is the observed acceleration vector and $\alpha$, $\beta$, and $\gamma$ are the attitude deviation angles about roll, pitch, and yaw, which are determined by the star tracker on board CHAMP. For the case of horizontal wind derivations, the vertical component can be safely neglected. This is regarded reasonable since vertical winds are observed to within 10–40 m/s below auroral latitudes [*Smith*, 1998]. This also effectively avoids the complication caused by the unreliable measurement of vertical acceleration component [*Perosanz et al.*, 2003, 2005].

[43] The horizontal components of $\vec{a}$ obtained in this way can now be used to deduce the cross-track wind as described in section 2.1 of the main text.

[44] **Acknowledgments.** We thank J. Oberheide for helpful discussion on atmospheric tides. H. Liu is supported by the Japan Society for the Promotion of Science (JSPS). S. Watanabe is supported by the International Communication Foundation (ICF). We appreciate the operational support of the CHAMP mission by the German Aerospace Center (DLR) and the financial support for the data processing by the Federal Ministry of Education and Research (BMBF).

[45] Arthur Richmond thanks John Meriwether and another reviewer for their assistance in evaluating this paper.

## References

Balsley, B. B., B. G. Fejer, and D. T. Farley (1976), Radar measurements of neutral winds and temperatures in the equatorial E region, *J. Geophys. Res.*, *81*, 1457–1459.

Behnke, R. A., M. Kelley, G. Gonzales, and M. Larsen (1985), Dynamics of the arecibo ionosphere: A case study approach, *J. Geophys. Res.*, *90*, 4448–4452.

Biondi, M. A., B. G. Fejer, and S. A. Gonzalez (1990), Seasonal variations in the equatorial thermospheric wind measured at Arequipa, Peru, *J. Geophys. Res.*, *95*, 12,243–12,250.

Biondi, M. A., S. Y. Sazykin, B. G. Fejer, J. W. Meriwether, and C. G. Fesen (1999), Equatorial and low latitude thermospheric winds: Measured quiet time variations with season and solar flux from 1980 to 1990, *J. Geophys. Res.*, *104*, 17,091–17,106.

Bittencourt, J. A., and B. A. Tinsley (1976), Tropical F region winds from O I 1356-A and O I 6300-A emissions: 1. Theory, *J. Geophys. Res.*, *81*, 3781–3785.

Blanc, M., and A. D. Richmond (1980), The ionospheric disturbance dynamo, *J. Geophys. Res.*, *85*, 1669–1686.

Brekke, A., S. Nozawa, and T. Sparr (1994), Studies of the E region neutral wind in the quiet auroral ionosphere, *J. Geophys. Res.*, *99*, 8801–8825.

Burnside, R. G., and C. A. Tepley (1989), Optical observations of thermospheric neutral winds at Arecibo between 1980 and 1987, *J. Geophys. Res.*, *94*, 2711–2716.

Cho, H. R., and K. C. Yeh (1970), Neutral winds and the behavior of the ionospheric F2 region, *Radio Sci.*, *5*, 881–894.

Coley, W. R., R. A. Heelis, and N. W. Spencer (1994), Comparison of low-latitude ion and neutral zonal drift using DE2 data, *J. Geophys. Res.*, *99*, 341–348.

Emery, B. A. (1978), Neutral thermospheric winds deduced above Millstone Hill: 1. Mathematical model, uncertainties, and representative results, *J. Geophys. Res.*, *83*, 5691–5703.

Emmert, J. T., B. G. Fejer, G. G. Shepherd, and B. H. Solheim (2001), Climatology of middle- and low-latitude daytime F region disturbance neutral winds measured by Wind Imaging Interferometer (WINDII), *J. Geophys. Res.*, *106*, 24,701–24,712.

Emmert, J. T., B. G. Fejer, G. G. Shepherd, and B. H. Solheim (2002), Altitude dependence of middle and low-latitude daytime thermospheric disturbance winds measured by windii, *J. Geophys. Res.*, *107*(A12), 1483, doi:10.1029/2002JA009646.

Emmert, J. T., B. G. Fejer, G. G. Shepherd, and B. H. Solheim (2004), Average nighttime F region disturbance neutral winds measured by UARS WINDII: Initial results, *Geophys. Res. Lett.*, *31*, L22807, doi:10.1029/2004GL021611.

Fejer, B. G., C. A. Gonzales, D. T. Farley, M. C. Kelley, and R. F. Woodman (1979), Equatorial electric fields during magnetically disturned conditions 1. The effect of the interplanetary magnetic field, *J. Geophys. Res.*, *84*, 5797–5802.

Fejer, B. G., D. T. Farley, C. A. Gonzales, R. F. Woodman, and C. Calderon (1981), F region east-west drifts at Jicamarca, *J. Geophys. Res.*, *86*, 215–218.

Fejer, B. G., E. R. de Paula, S. A. Gonzales, and R. F. Woodman (1991), Average vertical and zonal F region plasma drifts over Jicamarca, *J. Geophys. Res.*, *96*, 13,901–13,906.

Fejer, B. G., J. T. Emmert, G. G. Shepherd, and B. H. Solheim (2000), Average daytime f region disturbance neutral winds measured by uars: Initial results, *Geophys. Res. Lett.*, *27*, 1859–1862.

Fejer, B. G., J. T. Emmert, and D. P. Sipler (2002), Climatology and storm time dependence of nighttime thermospheric neutral winds over Millstone Hill, *J. Geophys. Res.*, *107*(A5), 1052, doi:10.1029/2001JA000300.

Fesen, C. G. (1996), Simulations of the low-latitude midnight temperature maximum, *J. Geophys. Res.*, *101*, 26,863–26,874.

Forbes, J. M., R. G. Roble, and F. A. Marcos (1993), Magnetic activity dependence of high-latitude thermospheric winds and densities below 200 km, *J. Geophys. Res.*, *98*, 13,693–13,702.

Förste, C., and S. Choi (2004), CHAMP accelerometer preprocessing at GeoForschungsZentrum Potsdam, in *Earth Observation With CHAMP*, edited by C. Reigber et al., pp. 169–174, Springer, New York.

Fuller-Rowell, T. J., M. V. Codrescu, R. J. Moffett, and S. Quegan (1994), Response of the thermosphere and ionosphere to geomagnetic storms, *J. Geophys. Res.*, *99*, 3893–3914.

Fuller-Rowell, T. J., M. V. Codrescu, H. Rishbeth, R. J. Moffett, and S. Quegan (1996), On the seasonal response of the thermosphere and ionosphere to geomagnetic storms, *J. Geophys. Res.*, *101*, 2343–2353.

Gaposchkin, E. M. (2003), Atmospheric superrotation?, *Planet. Space Sci.*, *51*, 415–425.

Hedin, A. E., et al. (1991), Revised global model of thermosphere winds using satellite and ground-based observations, *J. Geophys. Res.*, *96*, 7657–7688.

Hedin, A. E., et al. (1996), Empirical wind model for the upper, middle and lower atmosphere, *J. Atmos. Sol. Terr. Phys.*, *58*, 1421–1447.

Herrero, F. A., H. G. Mayr, N. W. Spencer, A. E. Hedin, and B. G. Fejer (1985), Interaction of zonal winds with the equatorial midnight pressure bulge in the Earth's thermosphere: Empirical check of momentum balance, *Geophys. Res. Lett.*, *12*, 491–494.

Kelley, M. C. (1989), *The Earth's Ionosphere*, Elsevier, New York.

Killeen, T. L., J. J. Ponthieu, J. D. Craven, L. A. Frank, and N. W. Spencer (1988), On the relationship between dynamics of the polar thermosphere and morphology of the aurora - global-scale observations from Dynamics Explorers 1 and 2, *J. Geophys. Res.*, *93*, 2675–2692.

King-Hele, D. G. (1964), The rotational speed of the upper atmosphere determined from changes in satellite orbits, *Planet. Space Sci.*, *12*, 835–853.

King-Hele, D. G., and D. M. C. Walker (1983), Upper-atmosphere zonal winds from satellite orbit analysis, *Planet. Space Sci.*, *31*, 509–535.

Liu, H., H. Lühr, V. Henize, and W. Köhler (2005), Global distribution of the thermospheric total mass density derived from CHAMP, *J. Geophys. Res.*, *110*, A04301, doi:10.1029/2004JA010741.

Marcos, F. A., and J. M. Forbes (1985), Thermospheric winds from the satellite electrostatic triaxial accelerometer system, *J. Geophys. Res.*, *90*, 6543–6552.

Maynard, N. C., T. L. Aggson, F. A. Herrero, and M. C. Liebrecht (1988), Average low-latitude meridional electric fields from DE2 during solar maximum, *J. Geophys. Res.*, *93*, 4021–4037.

Meriwether, J. W. J., J. W. Moody, M. A. Biondi, and R. G. Roble (1986), Optical interferometric measurements of nighttime equatorial thermospheric winds at Arequipa, Peru, *J. Geophys. Res.*, *91*, 5557–5566.

Meriwether, J. W. J., M. A. Biodi, F. A. Herrero, C. G. Fesen, and D. C. Hallenback (1997), Optical interferometric studies of the nighttime equatorial thermosphere: Enhanced temperatures and zonal wind gradients, *J. Geophys. Res.*, *102*, 20,041–20,058.

Perosanz, R., et al. (2003), On board evaluation of the STAR accelerometer, in *First CHAMP Mission Results for Gravity, Magnetic and Atmospheric Studies*, edited by C. Reigber, H. Lühr, and P. Schwintzer, pp. 11–18, Springer, New York.

Perosanz, R., R. Biancale, J. M. Lemoine, N. Vales, S. Loyer, and S. Bruinsma (2005), Evaluation of the CHAMP accelerometer on two years of mission, in *Earth Observation With CHAMP*, edited by C. Reigber et al., pp. 77–82, Springer, New York.

Richmond, A. D., and R. G. Roble (1987), Electrodynamic effects of thermospheric winds from the NCAR thermospheric general circulation model, *J. Geophys. Res.*, *92*, 12,365–12,376.

Richmond, A. D., S. Matsushita, and J. D. Tarpley (1976), On the production mechanism of electric currents and fields in the ionosphere, *J. Geophys. Res.*, *81*, 547–555.

Rishbeth, H. (1972a), Superrotation of the upper atmosphere, *Rev. Geophys.*, *10*, 799–819.

Rishbeth, H. (1972b), Thermospheric winds and the F-region: A review, *J. Atmos. Terr. Phys.*, *34*, 1–47.

Rishbeth, H. (2002), Whatever happened to superrotation, *J. Atmos. Sol. Terr. Phys.*, *64*, 1351–1360.

Sipler, D. P., M. A. Biondi, and R. G. Roble (1983), F-region neutral winds and temperatures at equatorial latitudes: Measured and predicted behavior during geomagnetically quiet conditions, *Planet. Space Sci.*, *31*, 53–66.

Smith, R. W. (1998), Vertical winds: A tutorial, *J. Atmos. Terr. Phys.*, *60*, 1425–1434.

Spencer, N. W., L. E. Wharton, H. B. Niemann, A. E. Hedin, G. R. Carignan, and J. C. Maurer (1981), The Dynamics Explorer wind and temperature spectrometer, *Space Sci. Instrum.*, *5*, 417–428.

Tapley, B., S. Bettadpur, M. Watkins, and C. Reigber (2004), The gravity recovery and climate experiment: Mission overview and early results, *Geophys. Res. Lett.*, *31*, L09607, doi:10.1029/2004GL019920.

Visser, P. N. A. M., and J. van den IJssel (2003), Verification of CHAMP accelerometer observations, *Adv. Space Res.*, *31*, 1905–1910.

Wharton, L. E., N. W. Spencer, and H. G. Mayr (1984), The earth's thermospheric superrotation from Dynamics Explorer 2, *Geophys. Res. Lett.*, *11*, 531–533.

Wu, Q., T. L. Killeen, and N. W. Spencer (1994), Dynamics Explorer 2 observations of equatorial thermospheric winds and temperatures: Local time and longitudinal dependences, *J. Geophys. Res.*, *99*, 6277–6288.

H. Liu and S. Watanabe, Division of Earth and Planetary Science, Hokkaido University, Sapporo 060-0810, Japan. (huixin@ep.sci.hokudai.ac.jp)

H. Lühr, W. Köhler, and V. Henize, GeoForschungZentrum Potsdam, 14473 Potsdam, Germany.

P. Visser, Department of Earth Observation and Space Systems, Delft University of Technology, Kluyverweg 1, 2629 HS, Delft, Netherlands.